Flexible and Printed Electronics

oe-a KFPE Korea Flexible & Printed Electronics Society PURPOSE-LED PUBLISHING™

PAPER • OPEN ACCESS

Electromagnetic interference shielding in soft, lightweight, and flexible conducting polymer-based sponges

To cite this article: Biporjoy Sarkar *et al* 2025 *Flex. Print. Electron.* **10** 025002

View the article online for updates and enhancements.

You may also like

- Recent progress of flexible pressure sensors: from principle, structure to application characteristics
Shimin Liu, Guilei Liu, Jianlong Qiu et al.

- Flexible and stretchable synaptic devices for wearable neuromorphic electronics
Hyeon-Soo Lee, Jun-Seok Ro, Gyu-Min Ko et al.

- Relationship between deposition techniques and nanoparticle dispersions for flexible and printed electronics
P Q Oliveira, R Arbi, M Munir et al.

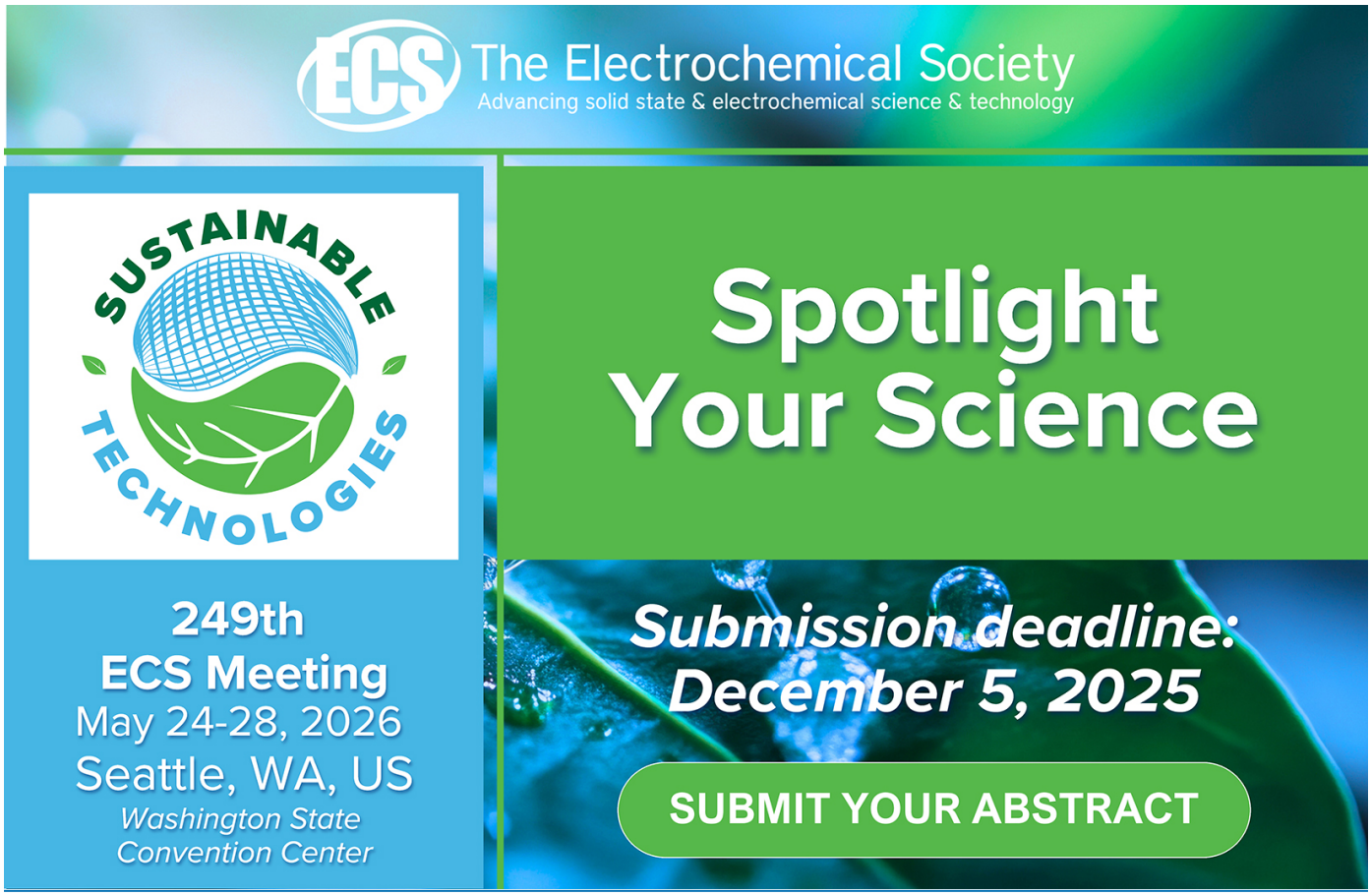

This content was downloaded from IP address 132.207.88.84 on 28/10/2025 at 13:10

IOP Publishing Flex. Print. Electron. 10 (2025) 025002 https://doi.org/10.1088/2058-8585/adc589

Flexible and Printed Electronics

CrossMark

OPEN ACCESS

RECEIVED
28 October 2024

REVISED
10 February 2025

ACCEPTED FOR PUBLICATION
26 March 2025

PUBLISHED
3 April 2025

Original content from this work may be used under the terms of the Creative Commons Attribution 4.0 licence.

Any further distribution of this work must maintain attribution to the author(s) and the title of the work, journal citation and DOI.

PAPER

Electromagnetic interference shielding in soft, lightweight, and flexible conducting polymer-based sponges

Biporjoy Sarkar[1,2], **Floriane Miquet-Westphal**[1], **Jiaxin Fan**[1], **Gayaneh Petrossian**[1] **and Fabio Cicoira**[1,*]

[1] Department of Chemical Engineering, Polytechnique Montreal, Montreal H3T 1J4, Canada
[2] MIE-Chemistry, Biology and Innovation (CBI) UMR8231, ESPCI Paris, CNRS, PSL Research University, 10 rue Vauquelin, 75005 Paris, France
[*] Author to whom any correspondence should be addressed.

E-mail: fabio.cicoira@polymtl.ca

Keywords: PEDOT:PSS sponges, mechanical properties, electromechanical response, EMI shielding

Supplementary material for this article is available online

Abstract

Developing highly efficient, low-density, and mechanically flexible electromagnetic interference (EMI) shielding materials based on conducting polymers has gained significant momentum for suppressing electromagnetic pollution. In our work, we investigated the EMI shielding behavior of uniaxially compressible sponges using the conducting polymer poly(3,4-ethylenedixoythiophene) polystyrene sulfonate (PEDOT:PSS) in the X-band frequency range of 8–12.4 GHz. Two types of PEDOT:PSS sponges, type-I with glycerol and (3-glycidyloxypropyl) trimethoxy silane and type-II containing glycerol and polyethylene glycol, were prepared by freeze-drying method. Both sponges exhibited a rapid decrease in resistance for the initial compressive strain of less than 20%, which stabilized at higher compressive strains. This behavior was likely due to the complex 3D porous structures of the sponges and was linked to the creation of new electrical contacts due to pore collapse under compressive strain. The enhanced electrical conductivity, porous structure, large surface area, and many internal surfaces resulted in exceptional EMI shielding for PEDOT:PSS sponges, achieving shielding values as high as 44 dB and 72 dB, respectively. The EMI shielding in these materials was primarily dominated by the reflection process. This work contributes to developing flexible and high-efficiency EMI shielding materials for flexible electronic applications in the future.

1. Introduction

The escalating use of wireless telecommunication technology has resulted in a rise in electromagnetic pollution, which has detrimental impacts on its surrounding electronic components and human health [1–9]. In particular, for X-band frequency range (8–12.4 GHz), which is often used in telecommunication and military applications, electromagnetic interference (EMI) shielding is essential. Metals are widely used for EMI shielding due to their high electrical conductivity, but concurrently, they offer several disadvantages, including complex processing from minerals, susceptibility to corrosion, high mass density, hardness, and relatively high cost [10]. The EMI shielding in a material occurs via reflection, absorption, and multiple reflections [11–13]. The mathematical relationship between total shielding efficiency (SE_T), electrical conductivity, and thickness of the material can be expressed by the Simon formula as follows:

$$SE_T = 50 + 10\log\left(\frac{\sigma}{f}\right) + 1.7t\sqrt{\sigma f} \quad (1)$$

where σ (S cm^{-1}), t (m), and f (MHz) are the electrical conductivity, material thickness, and frequency, respectively [14]. Additionally, the SE for the absorption (SE_A) and reflection (SE_R) can be calculated with:

$$SE_R = 50 + 10\log\left(\frac{\sigma}{f}\right) \quad (2)$$

$$SE_A = 1.7t\sqrt{\sigma f}. \quad (3)$$

© 2025 The Author(s). Published by IOP Publishing Ltd

Along with excellent EMI SE, other attributes such as ease-of-processing, lightweight, and mechanical flexibility are particularly important for applications in emerging areas such as aerospace, military, and wearable electronics [15]. Interestingly, conducting polymers meet these criteria in addition to their tunable electrical conductivity, resistance against corrosion, biodegradability, and cost-effectiveness [16]. A low-density (0.28 g cm^{-3}) polypyrrole-based composite loaded with polydopamine and silver nanowire (0–50%) showed tunable SE between 6.5 dB and 48.4 dB due to a reflection-absorption process, together with excellent mechanical properties [17]. Low density (0.57 g cm^{-3}) polymer poly(3,4-ethylenedixoythiophene) polystyrene sulfonate (PEDOT:PSS) films cross-linked with divinyl sulfone exhibited a SE value of 40 dB, which mostly resulted from the absorption process [18]. Recently, porous materials have gained considerable popularity for lightweight EMI shielding applications [19–23]. For instance, ultralow density (5 mg cm^{-3}) 3D hollow skeleton structured composite foam comprising 3 wt% MXene and carbon revealed an EMI SE value larger than 25 dB in the X-band frequency [24].

Complex synthesis methods are often employed to enhance EMI efficiency in PEDOT:PSS-based shielding materials. For instance, carbon dots and tellurium rods are processed with microwave and chemical reduction, and are mixed with PEDOT:PSS as nanofillers ranging from 0–10 wt%, they exhibit an EMI SE value of about 63 dB at an optimum concentration of 8 wt%, primarily due to an absorption process [25]. These PEDOT:PSS films are reported to have prospective applications in microwave shielding, biological fields, and wearable electronics. A PEDOT:PSS-$InCl_3$/10.9 mol% hydrogel was developed through a complex synthesis process, resulting in a high specific shielding effectiveness (SE) of 1425 dB mm^{-1} [26]. These hydrogel films effectively mitigate EM waves generated by a Tesla coil operating at a frequency of 50 Hz. Thick stretchable composite films made from (Li-TFSI)-doped (PEDOT:PSS), combined with ethylene glycol and carboxylated styrene-butadiene rubber (XSB) latex demonstrated a maximum EMI SE of 50 dB, indicating the potential for stretchable electronics application [27]. However, the EMI SE value of these composite films decreased significantly when stretched. Recently, an ultra-broadband EMI shielding material was developed using a cross-linked bi-hierarchical porous structure influenced by the dimethyl sulfoxide ratio (DMSO) ratio and tunable hydrogen bonds, utilizing an artificially re-structured PEDOT:PSS/konjac glucomannan, which exhibited a high EMI SE of about 58 dB in the range of 0.2–4 THz [28].

While there are reports on various conducting polymer-based EMI shielding, but the sponges have not been widely investigated. Conventional experimental methods such as drop-casting, spin-coating, and solution-casting for making PEDOT:PSS films pose limitations in EMI shielding applications primarily due to the dense structures of the resulting films, which exhibit minimal porosity and are incapable of effectively scattering and absorbing incoming EM waves [29–31]. In contrast, the novel and straightforward freeze-drying method enables the formation of a hierarchical porous structure, amplifying interfacial attenuation by increasing surface area and significantly improving EMI shielding properties. This process also substantially reduces the weight of the polymer and improves its mechanical flexibility. Therefore, the freeze-drying method could be an effective approach for developing PEDOT:PSS sponges suitable for EMI shielding and pressure sensing applications. Our previous work demonstrated PEDOT:PSS sponges without additives achieved a maximum EMI SE of about 15 dB, coupled with a very high porosity of 96% [32]. Even after compressing these sponges and consequently reducing their porosity, the EMI SE improved by about 60% of the original value. However, these results are still insufficient for high-end EMI shielding applications, which generally require EMI SE values between 40–120 dB. To address these challenges, we explored the EMI shielding properties of PEDOT:PSS sponges by modifying their porosity through various additives. In this study, we successfully enhanced the EMI SE values of PEDOT:PSS sponges to about 44 and 72 dB, with the incorporation of certain additives.

This work investigated the EMI shielding properties of low-density and flexible PEDOT:PSS sponges in the X-band frequency range between 8–12.4 GHz. Two types of PEDOT:PSS sponges, revealing 3D complex porous structure, demonstrated excellent electromechanical response due to enhanced electrical conductivity by pore collapse. On the contrary, excellent SE values of ∼44 dB and 72 dB for the two sponges can be attributed to their high electrical conductivities, porous structures, large surface areas, and many internal surfaces.

2. Experimental section

2.1. Materials

PEDOT:PSS (Clevios PH1000) was purchased from Heraeus Electronic Materials GmbH (Leverkusen, Germany). A centrifugal mixer (THINKY ARM-310) was used to prepare a uniform dispersion of PEDOT:PSS by vigorously stirring at 2000 rpm for 3 min. Glycerol, polyethylene glycol 400 (PEG-400), and (3-glycidyloxypropyl) trimethoxy silane (GOPS)

were purchased from Sigma Aldrich and subsequently used as-received without further purification.

2.2. PEDOT:PSS sponges preparation

Two different processing mixtures were used for sponges preparation: (i) PEDOT:PSS/5% glycerol/0.5% GOPS (type-I), and (ii) PEDOT:PSS/4% glycerol/5% PEG-400 (type-II). The varying concentrations of additives were measured relative to PEDOT:PSS dispersion. The uniform mixtures of PEDOT:PSS (10 ml) were prepared by vigorously stirring at 2000 rpm for 3 min. Next, the mixtures were transferred in centrifugal tubes and Petri dish and stored in a freezer (Sanyo, model no: MDF-U74V) at −20 °C for 27 h. Then, the frozen samples were moved to a freeze-dryer (Labconco, model: Freezone 2.5 Plus) at −80 °C again for 27 h to finalize the preparation of PEDOT:PSS sponges. Small amount of GOPS (0.5 wt%) may increase the mechanical integrity in type-I sponges [33]. For the type-II sponges, adding 5 wt% PEG-400 could increase its elastic properties, thereby impacting its overall mechanical compressibility.

3. Characterization

3.1. Density measurement

The weight of two PEDOT:PSS sponges was measured using an analytical balance having a resolution of 0.1 mg (AL 104, Mettler Toledo). The average thickness of the freeze-dried PEDOT:PSS sponges were measured to be ∼0.4 mm, which were then cut into a square shape of a length 4.07 mm and a breadth 5.16 mm. The volume of the sponges was calculated using the formula: length × breadth × height (in cm^3). Finally, the weight was divided by the volume of the sponges to estimate the density (see table 1).

Table 1. Density of PEDOT:PSS based sponges. The errors for thickness and density were calculated from measurements on at least three similar samples.

Materials	Thickness (mm)	Density (g cm^{-3})
Type-I sponges	0.4 ± 0.02	0.63 ± 0.24
Type-II sponges	0.4 ± 0.04	0.92 ± 0.14

3.2. Scanning electron microscopy (SEM)

The surface images of PEDOT:PSS type-I sponges and type-II sponges were obtained using a SEM (Hitachi TM3030) in a mixed mode (secondary and back scattered secondary electron) at ambient conditions.

3.3. Mechanical properties

The mechanical properties of the samples were tested using a multi-axial mechanical tester (Mach-1 model v500csst, Biomomentum, Canada) equipped with a load cell.

3.3.1. Compressive stress-strain measurement:
Cylindrical PEDOT:PSS sponges were placed on the stage of the multi-axial tester and compressed at a speed of 0.2 mm s^{-1} until squeezed completely under the movable load cell. A vertical force was applied on the sponges. The compressive Young's modulus of PEDOT:PSS sponges was calculated using the following equation:

$$E = \text{slope} \times (\text{thickness/area}). \tag{4}$$

The slope was calculated from the linear elastic region of the stress-strain curve.

3.4. Electro-mechanical measurement

Electrical response under uniaxial compression was measured using an electrical source meter (Agilent B2902A) together with a linear tensile/compression setup. The sponges were sandwiched between the electrodes attached with two ends of the linear tensile/compression setup during compression. The normalized resistance (expressed in percentage) was denoted as:

$$\frac{\Delta R}{R} = \frac{R_0 - R}{R_0} \tag{5}$$

where R_0 and R represent the resistance at zero and non-zero compression, respectively.

3.5. Electromagnetic shielding interference measurement

The complex scattering (S) parameters were obtained using a vector network analyzer (Keysight PNA-X N5247B), introducing WR 90 waveguide of dimension 22.86 mm × 10.16 mm, in the X-band frequency range between 8–12.4 GHz at room temperature. Two port calibration (Thru-Reflect-Line) was performed before starting the actual measurements. The SE, expressed in decibels (dB), can be defined as the logarithmic ratio of incident and transmitted power as follows:

$$SE_T = 10 \log\left(\frac{P_i}{P_t}\right) \tag{6}$$

where P_i and P_t are the incident and transmitted power. The total SE (SE_T) can be denoted as the algebraic sum of reflection (SE_R), absorption (SE_A), and multiple reflection (SE_{MR}) [8, 34–36],

$$SE_T = SE_R + SE_A + SE_{MR}\ SE_R + SE_A. \tag{7}$$

Based on the literature, SE_{MR} can be neglected when the magnitude of SE_T exceeds 15 dB [36–38]. The equations representing the correlation between SE, reflection coefficient, and absorption coefficient can be written as:

$$SE_R = -10 \log(1 - R) \tag{8}$$

$$SE_A = -10 \log\left(\frac{T}{1-R}\right) \quad (9)$$

$$SE_T = -10 \log T. \quad (10)$$

Finally, the shielding efficiency, expressed in percentage, can be referred to in the following equation [18]:

$$\text{EMI shielding efficiency } (\%) = 100 - \left(\frac{1}{10^{\frac{SE_T}{10}}}\right) \times 100. \quad (11)$$

4. Results and Discussion

Firstly, we prepared two PEDOT:PSS sponges, type-I and type-II, using a freeze-drying technique, with varying additives combinations. The freeze-drying facilitated the formation of the porous structure of the materials through two successive steps: (i) freezing the polymer dispersion at −20 °C and (ii) freeze-drying at −80 °C via sublimation.

The schematic representation of PEDOT:PSS sponges preparation using freeze-drying, combined with key experimental techniques involved in the characterization processes, is shown in figure 1. Mixing PEDOT:PSS with glycerol, GOPS, and PEG-400 can lead to several effects. Glycerol, which contains three hydroxyl (-OH) groups, engages in hydrogen bonding, dipole–dipole interactions, and dipole-charge interactions with the sulfonic acid (-SO_3H) groups of PSS layers, resulting in a stronger affinity toward PSS layers compared to PEDOT. During this process, condensation reactions occur between the -OH groups of glycerol and the -SO_3H groups of PSS, leading to the formation of sulfonic ester (S–O–C) bonds via covalent linkage [39]. When GOPS is added to PEDOT:PSS, two types of interactions take place: the epoxy rings of GOPS interact with the -SO_3H groups of PSS layers, and GOPS-GOPS interactions occur via methoxy silane groups [40]. The interactions between PEG and PEDOT:PSS are primarily governed by the formation of hydrogen bonds with PSS layers resulting in a transformation from core–shell to quasi-linear structures [41]. The results are also illustrated in figure 1. Figures 2(a) and (b) demonstrate the complex 3D porous structure of both types of sponges, with irregular pore shapes and sizes distributed randomly. The pore structure in freeze-dried sponges is influenced by factors such as freezing temperature, types of additives, freezing direction, and additive concentration. When freezing occurs at a higher temperature (e.g. −20 °C) than freeze-drying (e.g. −80 °C), ice nucleation is slower, leading to larger and randomly distributed pores [42]. In contrast, directional freeze-drying, achieved through a high-temperature gradient, allows controlled ice crystal growth, resulting in unidirectional pores. Since our freezing method does not involve such directional control, we do not expect a well-defined pore orientation or structure [42].

According to the literature, the mathematical relationship between porosity and density in a porous material is represented by equation (12) [43]. As porosity increases, the density of the porous material decreases.

$$\varphi = 1 - \frac{\rho_{\text{sponge}}}{\rho_{\text{bulk}}} \quad (12)$$

where ρ_{sponge} and ρ_{bulk} represent the sponges density and bulk density (without pores), respectively. The values of sponges densities are 0.63 ± 0.24 g cm^{-3} and 0.92 ± 0.14 g cm^{-3} for type-I and type-II sponges, respectively, while the value of ρ_{bulk} of PEDOT:PSS is approximately 1.03 g cm^{-3}. This equation estimates values φ of 38% for type-I and 9% for type-II, indicating that type-I has higher porosity than type-II sponges. We believe that glycerol, GOPS, and PEG-400 impact pore formation in PEDOT:PSS sponges by changing solution viscosity, degree of crosslinking, and viscoelastic behavior [40, 41, 44]. Glycerol may disrupt the hydrogen bonding arrangement in water, inhibiting ice formation, which resulted in smaller pores due to slower ice crystal growth [45]. GOPS may stabilize PEDOT:PSS by enabling crosslinking network, adding mechanical strength to the pores [40]. PEG-400 may reduce the elastic modulus of porous structure due to its high mobility and shorter polymer chains [44].

As noted, type-I contains GOPS and glycerol, while type-II has glycerol and PEG-400. It may be challenging to discuss the percolation threshold in the sponges due to the complex hybrid nature of the precursor materials, which is influenced by distinct percolation thresholds, their concentrations, and their interactions among different additives.

The stress-strain curves for type-I and type-II sponges subjected to compression are shown in figure 3(a). A representative schematic of the stress-strain curve of sponges is presented in Figure S1. The stress-strain curve for PEDOT:PSS sponges exhibited four distinct deformation regions: (i) linear elastic, (ii) elastic-to-plastic, (iii) plateau (plastic), and (iv) densification. At small strains (<2% for type-I and <5% for type-II), the sponges deformed elastically with a relatively a negligible deformation of the internal pores. As the load increased, we speculated that the pores in both types of samples began to collapse during the elastic-to-plastic transition region, which were 2%–10% for type-I sponges, and 5%–25% for type-II sponges. Subsequently, the collapse of the pores progressed at roughly constant load, leading to a stress plateau, which was approximately 10%–37% for type-I sponges, and 25%–63% for type-II sponges. At higher strains (37% for type-I sponges and 63% for type-II sponges), the opposing walls of the pores met and touched, resulting in a steep

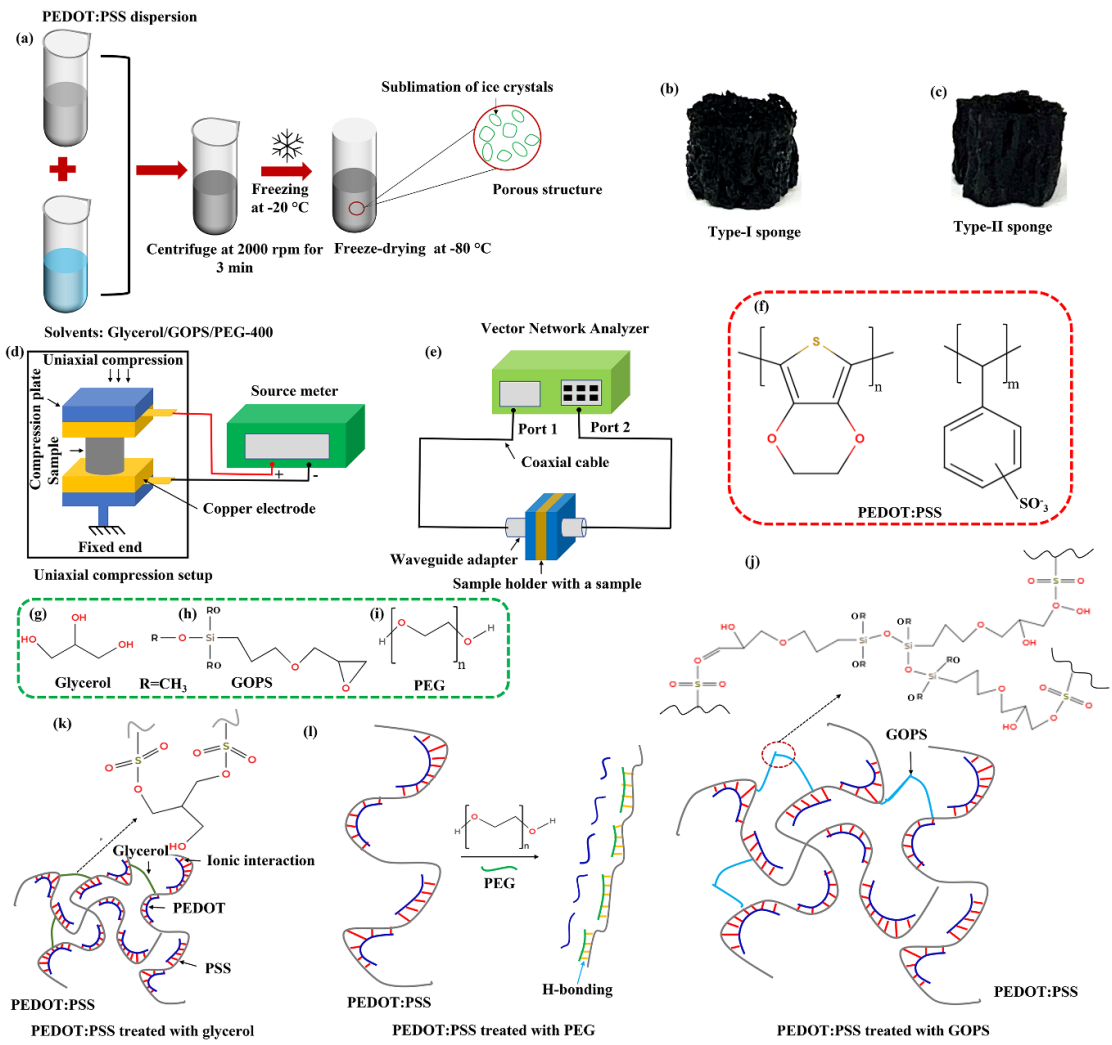

Figure 1. Schematic representation of (a) the process of obtaining cylindrical PEDOT:PSS sponges using a freeze-drying technique (b) a digital photograph of type-I freestanding PEDOT:PSS sponges (c) a digital photograph of type-II freestanding PEDOT:PSS sponges (d) experimental setup for the compressive stress-strain measurements coupled with an electrical source meter (e) experimental setup for the EMI shielding effectiveness measurement using a vector network analyzer. The schematic representation of chemical structure includes (f) PEDOT:PSS (g) glycerol (h) GOPS (i) PEG (j) crosslinking between PEDOT:PSS and GOPS (k) PEDOT:PSS crosslinked with glycerol (l) transformation from core–shell to quasi-linear structure via PEG treatment due to hydrogen bonding. The chemical reactions between glycerol and GOPS with PSS layers are also illustrated in the figure.

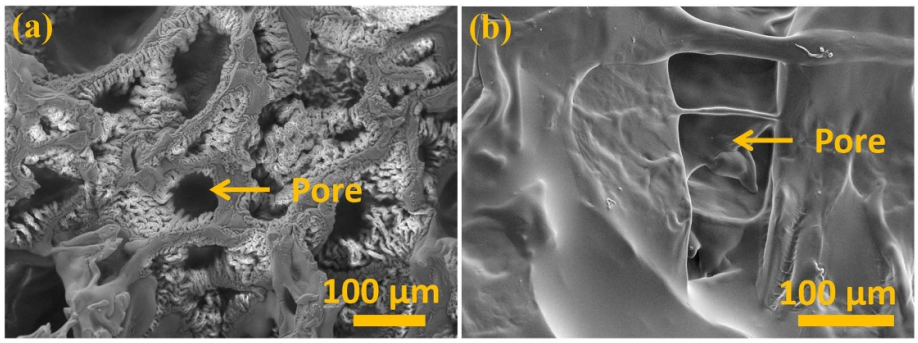

Figure 2. SEM images of (a) type-I PEDOT:PSS sponges and (b) type-II PEDOT:PSS sponges,

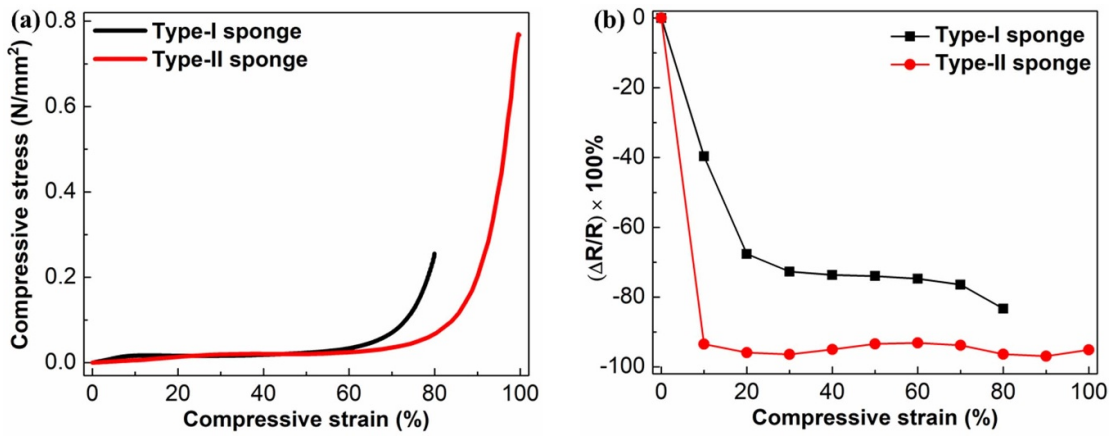

Figure 3. (a) Compressive stress-stain plot of type-I and type-II PEDOT:PSS sponges (b) normalized resistance ($(\Delta R/R)\times$ 100%) versus compressive strain plot for type-I and type-II PEDOT:PSS sponges. Black and red solid lines in figures (a) and (b) represented data points corresponding to type-I and type-II sponges.

rise in stress as the material densified. The densification region lasted up to nearly 80% and 100% compression for type-I and type-II sponges, respectively. These results indicated that type-I and type-II sponges exhibit compressive Young's moduli of 55.2 ± 8.4 kPa and 7.29 ± 1.12 kPa, respectively, revealing that type-II sponges has a notably softer structure compared to type-I sponges. The combination of 5% glycerol and 0.5% GOPS in type-I sponges facilitated the increase in Young's modulus primarily due to their strong crosslinking effects on PEDOT:PSS (as shown in figure 1). Conversely, in the type-II sponges, 4% glycerol solely acted as a crosslinker to enhance Young's modulus, whereas 5% PEG decreased it due to its viscoelastic properties [44]. It is important to note that the specified values of additive concentrations were selected to optimize their effect on the electrical and mechanical properties of PEDOT:PSS. Any deviation of these values might adversely impact these properties. The additive concentrations exceeding 0.5% for GOPS, 5% for glycerol, and 5% for PEG could lead to saturation in their electrical properties [40, 41, 46], likely resulting in a similar saturation in the mechanical properties.

Next, we assessed the evolution of resistance as a function of compression for type-I and type-II sponges, as shown in figure 3(b). The average bulk resistances of type-I and type-II sponges were estimated at 4.25 Ω and 61.53 Ω, respectively. We suggest that when the magnitude of compressive strain in PEDOT:PSS sponges is minimal, the deformation from compression shortens the conducting path between the walls of the pores without allowing them to touch. This causes a minimal decrease in electrical resistance [43]. When PEDOT:PSS sponges are under increasing compression, the pores begin to deform, resulting in increased contact area and reduced electrical resistance. When the compression reaches a critical value (20% for type-I and 10% for type-II sponges), the contact area increases further due to the closing of the pores, which enhances conductive pathways and steadily decreases electrical resistance. At 20% compression, the electrical resistances of type-I and type-II sponges decrease by about 70% and 95% of their initial values, respectively. Under extremely large compression, the pores are mostly collapsed in the sponges, leading to saturation in the electrical resistance [32, 44]. Notably, due to its lower Young's modulus, the type-II sponges exhibited a greater decrease in electrical resistance than that of the type-I sponges.

Finally, the EMI shielding properties type-I sponges, and type-II sponges were evaluated in the X-band frequency range. The coefficients of reflection (R), absorption (A), and transmission (T) for all the samples were calculated from scattering (S) parameters. R and A values were obtained as 0.96 and 0.04 for type-I sponges and 0.99 and 0.01 for type-II sponges (figure S2). The frequency dependence of SE_R, SE_A, and SE_T was plotted and indicated a nearly stable response for the studied samples across the whole range of X-band frequency (figures 4(a) and (b)). The SE_T values corresponding to type-I sponges, and type-II sponges were ∼ 44 dB and 72 dB, respectively. We further estimated the EMI shielding efficiency values of 99.996% and 99.999% for type-I and type-II sponges, respectively. It was clear that type-II sponges is the most effective in addressing EM pollution as indicated by its high value of SE_T of 72 dB. It was understood from the literature that EMI shielding materials can be divided into three categories based on their SE values: low with SE $<$ 10 dB, moderate with 10 dB $<$ SE $<$ 30 dB, and high with SE $>$ 30 dB [47]. Particularly for aerospace applications, the requirement of SE values lies between 40 dB and 120 dB [48]. The impact of pores on EMI shielding depends on their size, distribution, and irregularities. Irregular pores increase surface area

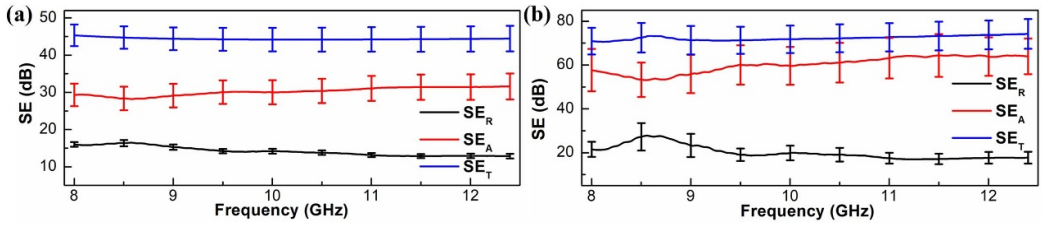

Figure 4. Variation of SE (SE_R, SE_A and SE_T) as a function of frequency for (a) type-I PEDOT:PSS sponges (b) type-II PEDOT:PSS sponges.

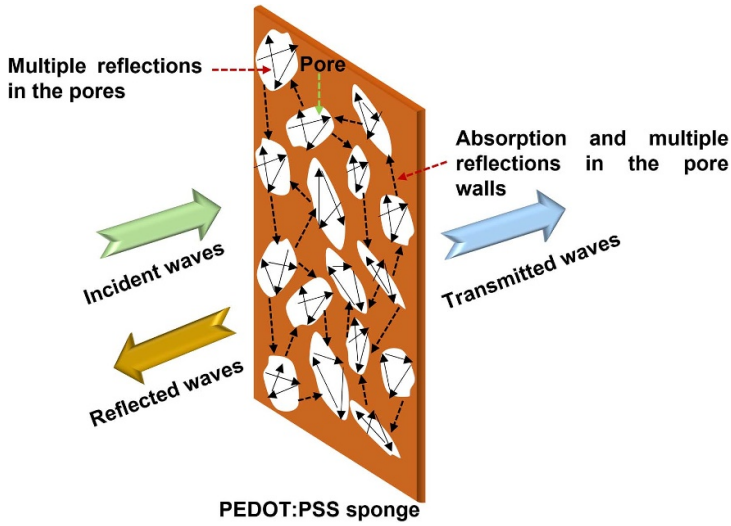

Figure 5. Schematic illustration of EMI shielding mechanism in PEDOT:PSS sponges.

and create intricate pathways, enhancing EMI shielding through internal scattering and multiple reflections. However, excessive irregularities can disrupt the conductive network, lowering electrical conductivity and SE. While pores play a key role, they are not the sole factor determining EMI shielding behavior. The EMI shielding due to reflection is determined by the impedance mismatch between air and PEDOT:PSS sponges [49, 50]. Given the high conductivity of these sponges, the reflection-based EMI shielding is anticipated to be considerable. EM waves attenuate as they penetrate the pore walls, depending on the wave impedance in the PEDOT:PSS sponges. Multiple reflections also occur between the two interfaces of the pore walls. As the EM waves transmit into the pores, they undergo both reflection and penetration upon arriving at the second interface. The reflected EM waves repeatedly bounce between the two interfaces within the pores, leading to prolonged wave propagation and increased energy dissipation through absorption and scattering [51]. However, excessive pore irregularities could negatively impact the internal conducting network, thereby reducing overall electrical conductivity, and resulting in a lower EMI SE. Overall, the high electrical conductivity, complex porous structure, large surface area, and the existence of many internal surfaces could result in attenuation of the EM waves in both sponges. The most probable mechanism for the EMI shielding in PEDOT:PSS sponges could be the combined effect of reflection and multiple internal reflection as they exhibited high R and high SE_A [52]. The presence of folded layered structure in type-II sponges in its cross-section (figure S3) contribute more to the interfacial attenuation of the incident EM waves that may result in higher value of EMI SE. The schematic illustration explaining EMI shielding mechanism in PEDOT:PSS sponges is shown in figure 5.

5. Conclusion

In the present study, we demonstrated the EMI shielding in PEDOT:PSS-based sponges in the X-band frequency range (8–12 GHz), together with their morphological, mechanical, and electromechanical characteristics. The compression-induced increase in the electrical response of 3D porous PEDOT:PSS sponges was attributed to the formation of new electrical contacts due to pore collapse. PEDOT:PSS sponges displayed excellent EMI SE values of 44 dB and 72 dB resulting from the combined effect of high electrical conductivity, porous

structure, large surface area, and interfacial attenuation of the EM waves. Our current work sheds light on designing lightweight and flexible EMI shielding materials, showing a wide range of SE values offering potential applications in portable electronic devices, aerospace, and military.

Data availability statement

The data cannot be made publicly available upon publication because they are not available in a format that is sufficiently accessible or reusable by other researchers. The data that support the findings of this study are available upon reasonable request from the authors.

Acknowledgment

This work was supported by DND NSERC discovery supplement and Defense Research and Development Canada through an IDEaS Micronet (CFPMN1-008) grant awarded to F.C. Equipment and infrastructure used for this research were acquired and maintained by NSERC, the Canada Foundation for Innovation and Quebec Strategic Networks (RQMP and CREPEC). JF acknowledges support from the NSERC postdoctoral fellowship. JF acknowledges NSERC for a postdoctoral fellowship. GP acknowledges NSERC for a Vanier Doctoral Scholarship. FMW acknowledges the Pierre Arbour Foundation for a Doctoral Scholarship.

Conflict of interest

The authors declare no conflict of interest.

ORCID iDs

Biporjoy Sarkar https://orcid.org/0000-0002-0978-0678
Gayaneh Petrossian https://orcid.org/0000-0002-7169-4869
Fabio Cicoira https://orcid.org/0000-0002-0047-608X

References

[1] Sarkar B, Miquet-Westphal F, Bobbara S, George B, Beltrame G, Dousset D, Wu K and Cicoira F 2023 Electromagnetic interference shielding in lightweight carbon xerogels *Mater. Res. Express* **10** 045601
[2] Tantawy H R, Aston D E, Smith J R and Young J L 2013 Comparison of electromagnetic shielding with polyaniline nanopowders produced in solvent-limited conditions *ACS Appl. Mater. Interfaces* **5** 4648–58
[3] Zhang L Q, Yang B, Teng J, Lei J, Yan D X, Zhong G J and Li Z M 2017 Tunable electromagnetic interference shielding effectiveness via multilayer assembly of regenerated cellulose as a supporting substrate and carbon nanotubes/polymer as a functional layer *J. Mater. Chem.* C **5** 3130–8
[4] Tian M, Du M, Qu L, Chen S, Zhu S and Han G 2017 Electromagnetic interference shielding cotton fabrics with high electrical conductivity and electrical heating behavior: via layer-by-layer self-assembly route *RSC Adv.* **7** 42641–52
[5] Lyu J, Zhao X, Hou X, Zhang Y, Li T and Yan Y 2017 Electromagnetic interference shielding based on a high strength polyaniline-aramid nanocomposite *Compos. Sci. Technol.* **149** 159–65
[6] Luo S J, Zhang P, Mei Y A, Chang J B and Yan H 2016 Electromagnetic interference shielding properties of PEDOT/PSS–halloysite nanotube (HNTs) hybrid films *J. Appl. Polym. Sci.* **133** 1–5
[7] Vyas M K and Chandra A 2016 Ion-electron-conducting polymer composites: promising electromagnetic interference shielding material *ACS Appl. Mater. Interfaces* **8** 18450–61
[8] Zhao B, Zhao C, Li R, Hamidinejad S M and Park C B 2017 Flexible, ultrathin, and high-efficiency electromagnetic shielding properties of poly(vinylidene fluoride)/carbon composite films *ACS Appl. Mater. Interfaces* **9** 20873–84
[9] Geetha S, Kumar K K S, Rao C R K, Vijayan M and Trivedi D C 2009 EMI shielding: methods and materials—a review *J. Appl. Polym. Sci.* **112** 2073–86
[10] Jiang D *et al* 2019 Electromagnetic interference shielding polymers and nanocomposites—a review *Polym. Rev.* **59** 280–337
[11] Wu Y, Wang Z, Liu X, Shen X, Zheng Q, Xue Q and Kim J K 2017 Ultralight graphene foam/conductive polymer composites for exceptional electromagnetic interference shielding *ACS Appl. Mater. Interfaces* **9** 9059–69
[12] Biswas S, Arief I, Panja S S and Bose S 2017 Absorption-dominated electromagnetic wave suppressor derived from ferrite-doped cross-linked graphene framework and conducting carbon *ACS Appl. Mater. Interfaces* **9** 3030–9
[13] Biswas S, Panja S S and Bose S 2017 Unique multilayered assembly consisting of "flower-like" ferrite nanoclusters conjugated with MWCNT as millimeter wave absorbers *J. Phys. Chem.* C **121** 13998–4009
[14] Bora P J, Anil A G, Ramamurthy P C and Tan D Q 2020 MXene interlayered crosslinked conducting polymer film for highly specific absorption and electromagnetic interference shielding *Mater. Adv.* **1** 177–83
[15] Zeng Z, Wang C, Siqueira G, Han D, Huch A, Abdolhosseinzadeh S, Heier J, Nüesch F, Zhang C and Nyström G 2020 Nanocellulose-MXene biomimetic aerogels with orientation-tunable electromagnetic interference shielding performance *Adv. Sci.* **7** 2000979
[16] Pradhan S S, Unnikrishnan L, Mohanty S and Nayak S K 2020 Thermally conducting polymer composites with EMI shielding: a review *J. Electron. Mater.* **49** 1749–64
[17] Wang Y, Gu F Q, Ni L J, Liang K, Marcus K, Liu S L, Yang F, Chen J J and Feng Z S 2017 Easily fabricated and lightweight PPy/PDA/AgNW composites for excellent electromagnetic interference shielding *Nanoscale* **9** 18318–25
[18] Bora P J, Anil A G, Vinoy K J and Ramamurthy P C 2019 Outstanding absolute electromagnetic interference shielding effectiveness of cross-linked PEDOT:PSS film *Adv. Mater. Interfaces* **6** 1901353
[19] Chen Z, Xu C, Ma C, Ren W and Cheng H M 2013 Lightweight and flexible graphene foam composites for high-performance electromagnetic interference shielding *Adv. Mater.* **25** 1296–300
[20] Wan C and Li J 2016 Graphene oxide/cellulose aerogels nanocomposite: preparation, pyrolysis, and application for electromagnetic interference shielding *Carbohydrate Polym.* **150** 172–9
[21] Li Y, Shen B, Pei X, Zhang Y, Yi D, Zhai W, Zhang L, Wei X and Zheng W 2016 Ultrathin carbon foams for effective electromagnetic interference shielding *Carbon* **100** 375–85
[22] Yan D X, Ren P G, Pang H, Fu Q, Yang M B and Li Z M 2012 Efficient electromagnetic interference shielding of lightweight graphene/polystyrene composite *J. Mater. Chem.* **22** 18772–4
[23] Sun X, Liu X, Shen X, Wu Y, Wang Z and Kim J K 2016 Graphene foam/carbon nanotube/poly(dimethyl siloxane)

composites for exceptional microwave shielding Composite A **85** 199–206
[24] Lu Y, Zhao X, Lin Y, Li P, Tao Y, Wang Z, Ma J, Xu H and Liu Y 2023 Lightweight MXene/carbon composite foam with hollow skeleton for air-stable, high-temperature-resistant and compressible electromagnetic interference shielding *Carbon* **206** 375–82
[25] Al Naim A F, Ibrahim S S and El-Shamy A G 2021 A new class of electromagnetic shields based on carbon dots adorning Te nanorods embedded into PEDOT:PSS for protection from electromagnetic (EM) pollutions *Prog. Org. Coat.* **161** 106486
[26] Wang H *et al* 2023 Multifunctional filler-free PEDOT:PSS hydrogels with ultrahigh electrical conductivity induced by lewis-acid-promoted ion exchange *Adv. Mater.* **35** 2302919
[27] Jiang X, Zhou J, Zhong X, Hu Z, Hu R, Song Y and Zheng Q 2023 Stretchable PEDOT:PSS/Li-TFSI/XSB composite films for electromagnetic interference shielding *ACS Appl. Mater. Interfaces* **15** 8521–8529
[28] Sun H, Wo Z, Su Y, Ma H and Zhang X 2023 An artificially re-structured PEDOT:PSS/konjac glucomannan sponges toward high-performance electromagnetic interference shielding from gigahertz to terahertz bands *J. Mater. Chem.* A **11** 21817–21827
[29] Jasna M, Pushkaran N K, Manoj M, Aanandan C K and Jayaraj M K 2020 Facile preparation of lightweight and flexible PVA/PEDOT:PSS/MWCNT ternary composite for high-performance EMI shielding in the X-band through absorption mechanism *J. Electron. Mater.* **49** 1689–701
[30] Yousefian H, Babaei-Ghazvini A, Isari A A, Alireza Hashemi S, Acharya B, Ghaffarkhah A and Arjmand M 2024 Solvent-doped PEDOT:PSS: structural transformations towards enhanced electrical conductivity and transferable electromagnetic shields *Surf. Interfaces* **51** 104481
[31] Hosseini E, Arjmand M, Sundararaj U and Karan K 2020 Filler-free conducting polymers as a new class of transparent electromagnetic interference shields *ACS Appl. Mater. Interfaces* **12** 28596–28606
[32] Sarkar B, Li X, Quenneville E, Carignan L P, Wu K and Cicoira F 2021 Lightweight and flexible conducting polymer sponges and hydrogels for electromagnetic interference shielding *J. Mater. Chem.* C **9** 16558–65
[33] ElMahmoudy M, Inal S, Charrier A, Uguz I, Malliaras G G and Sanaur S 2017 Tailoring the electrochemical and mechanical properties of PEDOT:PSS films for bioelectronics *Macromol. Mater. Eng.* **302** 1600497
[34] Li P, Du D, Guo L, Guo Y and Ouyang J 2016 Stretchable and conductive polymer films for high-performance electromagnetic interference shielding *J. Mater. Chem.* C **4** 6525–32
[35] Jung J, Lee H, Ha I, Cho H, Kim K K, Kwon J, Won P, Hong S and Ko S H 2017 Highly stretchable and transparent electromagnetic interference shielding film based on silver nanowire percolation network for wearable electronics applications *ACS Appl. Mater. Interfaces* **9** 44609–16
[36] Hong J *et al* 2023 Best practices for correlating electrical conductivity with broadband EMI shielding in binary filler-based conducting polymer composites *Chem. Eng. J.* **455** 140528
[37] Agnihotri N, Chakrabarti K and De A 2015 Highly efficient electromagnetic interference shielding using graphite nanoplatelet/poly(3,4-ethylenedioxythiophene)-poly(styrenesulfonate) composites with enhanced thermal conductivity *RSC Adv.* **5** 43765–71
[38] Basavaraja C, Noh G T and Huh D S 2013 Chemically modified polyaniline nanocomposites by poly(2-acrylamido-2-methyl-1-propanesulfonicacid)/graphene nanoplatelet *Colloid Polym. Sci.* **291** 2755–63
[39] Kim J, Jang J G, Kwak J, Hong J I and Kim S H 2019 Enhanced humid reliability of organic thermoelectrics via crosslinking with glycerol *Nanomaterials* **9** 1591
[40] Håkansson A, Han S, Wang S, Lu J, Braun S, Fahlman M, Berggren M, Crispin X and Fabiano S 2017 Effect of (3-glycidyloxypropyl)trimethoxysilane (GOPS) on the electrical properties of PEDOT:PSS films *J. Polym. Sci.* B **55** 814–20
[41] Alemu Mengistie D, Wang P C and Chu C W 2013 Effect of molecular weight of additives on the conductivity of PEDOT:PSS and efficiency for ITO-free organic solar cells *J. Mater. Chem.* A **1** 9907
[42] Qian L and Zhang H 2011 Controlled freezing and freeze drying: a versatile route for porous and micro-/nano-structured materials *J. Chem. Technol. Biotechnol.* **86** 172–84
[43] Kro¨ner J, Platzer D, Milowa B and Schwan M 2024 Electrical conductivity of monolithic and powdered carbon aerogels and their composites *Mater. Adv.* **5** 8042–52
[44] Li Y, Li X, Zhang S, Liu L, Hamad N, Bobbara S R, Pasini D and Cicoira F 2020 Autonomic self-healing of PEDOT:PSS achieved via polyethylene glycol addition *Adv. Funct. Mater.* **30** 2002853
[45] Alba-Simionesco C, Judeinstein P, Longeville S, Osta O, Porcher F, Caupin F and Tarjus G 2022 Interplay of vitrification and ice formation in a cryoprotectant aqueous solution at low temperature *Proc. Natl Acad. Sci.* **119** e2112248119
[46] Li J F, Zhao C, Zhang H, Tong J F, Zhang P, Yang C Y, Xia Y J and Fan D W 2015 Improving the performance of perovskite solar cells with glycerol-doped PEDOT:PSS buffer layer *Chin. Phys.* B **25** 028402
[47] Anon Space and Missile Systems Center 2008 Electromagnetic compatibility requirements for space equipment and systems,SMC standard SMC-S-008 air force space command El Segundo, CA
[48] Anon Afilipoaei C and Teodorescu-Draghicescu H 2020 A review over electromagnetic shielding effectiveness of composite materials *Proceedings* **63** 23
[49] Gao Q, Wang X, Schubert D W and Liu X 2024 Review on polymer/MXene composites for electromagnetic interference shielding applications *Adv. Nanocompos.* **1** 52–76
[50] Zheng S, Wang Y, Zhu Y and Zheng C 2024 Recent advances in structural design of conductive polymer composites for electromagnetic interference shielding *Polym. Compos.* **45** 43–76
[51] Xu Z and Hao H 2014 Electromagnetic interference shielding effectiveness of aluminum foams with different porosity *J. Alloys Compd.* **617** 292–301
[52] Hwang U, Kim J, Seol M, Lee B, Park I K, Suhr J and Nam J D 2022 Quantitative interpretation of electromagnetic interference shielding efficiency: is it really a wave absorber or a reflector? *ACS Omega* **7** 4135–9